The Role of Conical Intersections on the Efficiency of Fluorescent Organic Molecular Crystals

Miguel Rivera, Ljiljana Stojanović, and Rachel Crespo-Otero[*]

School of Biological and Chemical Sciences, Queen Mary University of London, Mile End Road, London, E1 4NS, U.K.

E-mail: r.crespo-otero@qmul.ac.uk

Abstract

Organic molecular crystals are attractive materials for luminescent applications due to their promised tunability. However, the link between chemical structure and emissive behaviour is poorly understood due to the numerous interconnected factors which are at play in determining radiative and non-radiative behaviours at the solid state level. In particular, the decay through conical intersection dominates the nonadiabatic regions of the potential energy surface, and thus their accessibility is a telling indicator of the luminosity of the material. In this study, we investigate the radiative mechanism for five organic molecular crystals which display solid state emission, with a focus on the role of conical intersections in their photomechanisms. The objective is to situate the importance of the accessibility of conical intersections with regards to emissive behaviour, taking into account other nonradiative decay channels, namely vibrational decay, and exciton hopping. We begin by giving a brief overview of the structural patterns of the five systems within a larger pool of thirteen crystals for a richer comparison. We observe that due to the prevalence of sheet-like and herringbone packing in organic

1

molecular crystals, the conformational diversity of crystal dimers is limited. Additionally, similarly spaced dimers have exciton coupling values of similar order within a 50 meV interval. Next, we focus on three exemplary cases, where we disentangle the role of nonradiative decay mechanisms and show how rotational minimum energy conical intersections in vacuum lead to puckered ones in crystal, increasing their instability upon crystallisation in typical packing motifs. In contrast, molecules with puckered conical intersections in vacuum tend to conserve this trait upon crystallisation, and therefore their quantum yield of fluorescence is determined predominantly by other nonradiative decay mechanisms.

1 Introduction

Organic molecular crystals represent a promising family of materials for optical applications such as light-emitting diodes[1] or lasing.[2] One of their major appeals is their tuneability, which is due to the large reorganisations in crystal conformation that can emerge from small alterations to molecular structure. The, often local,[3] excitations can radically change character due to their immediate environment. Thus, crystallisation is a potential cause of changes in photochemical material properties such as Stokes shift, polarisation or Quantum Efficiency of Fluorescence (QEF).[4]

To fully control the Solid State Luminescence (SSL) behaviour of these materials, the excited state radiative and non-radiative decay channels of the molecule need to be understood within a particular condensed phase environment. In particular, internal conversion through conical intersection is an ultrafast process which dominates photomechanisms in nonadiabatic regions of the potential energy surface (PES).

Controlling the accessibility of these regions upon crystallisation can produce luminescent crystals out of monomers which are less luminescent in solution or gas. This phenomenon of Solid State Luminescent Enhancement (SSLE)[5] requires the destabilisation of conical intersections—coined as the Restricted Access to Conical Intersections (RACI) model by Blancafort *et al.* in References 6 and 7—has successfully been applied to several

SSLE materials in the past.[8,9]

Internal conversion is also facilitated by a large overlap of vibrational wavefunctions between low energy vibrational modes (such as rotation or flapping) from the ground and excited states. These normal modes can be quenched upon crystallisation, thus blocking the nonradiative decay channel, and producing SSLE. This phenomenon is known as Restriction of Intramolecular Motions (RIM) model.[1,10]

SSLE systems must also avoid further nonradiative processes which arise in aggregates. In particular, delocalised exciton states (charge-transfer or otherwise), have an associated mobility mediated by the exciton hopping rate, rationalisable by Marcus theory. Highly mobile excitons can travel in the crystal to surfaces or defect sites, and undergo nonradiative processes there.[11]

Concretely, the balance between RACI, RIM and exciton transport effects is often assessed in a case-by-case basis for each SSLE crystal, due to the interconnectedness of the inter- and intramolecular factors which mediate each process. In this paper, we assess the pertinence of conical accessibility in explaining the luminescent response of five SSL crystals from three different molecular series. To characterise them in a broader context, we also offer a brief overview of the packing characteristics and excited state features of eight additional similar crystals, totalling the thirteen depicted in Figure 1. We aim to consider a large enough variety of systems that comparisons can be drawn between crystals with different degrees of packing and chemical similarity, and

The crystals were gathered into series based on their backbone structures and substituents. p-oligophenylenes (nP, n=3, 4, and 6) are a family of organic $\pi-$conjugated molecules composed of phenyl-rings attached to each other via single bonds in para-positions. The DCS series where three phenylene units are connected by vinylene bridges with cyano-group substituents, and additional buthoxy and methoxy groups are added to the backbone. We also consider the DSB molecule, which shares the same backbone but has no substituents and 4PV which further extends the phenylene chain by two phenylene

3

units. Additionally, we consider 2-(2'-hydroxyphenyl)benzothiazole (HBT), a molecule exhibiting excited state proton transfer in the solid state.

Barring certain substitutions of the DCS family and HBT, all systems display amplified spontaneous emission (ASE) in crystal, making them candidates for use as organic single crystal lasers, as detailed in Reference 4. All molecules undergo SSL,[5] some of it enhanced by crystallisation (SSLE).

The five crystals around which our investigation on conical intersections will revolve are chosen for their varied structural characteristics. They are HBT, α-DCS, 3P, 4P, and 6P. The first exhibits excited state intramolecular proton transfer (ESIPT), the second is the most emissive DCS crystal and has relatively large rotational flexibility, and the final three demonstrate the effect of chain length on their emissive character. The first two are SSLE materials whereas the nP series is also luminous in solution, giving us another property to compare.

We first present the computational details of our findings. Then, for the thirteen crystals, we analyse the geometric features of the crystal packing, and the excitonic coupling between constituent dimers. Then, we investigate the photomechanism of HBT, α-DCS, and the nP series focusing on their conical intersections. We complement our analysis with the investigation of other nonradiative decay channels beyond the RIR and RACI models.

2   Methods

The crystal structure geometries were optimised using PBE-D2 as implemented in `Quantum Espresso`,[12] with a basis set cut-off of 50 Ry and various Monkhorst-Pack Grids chosen in accordance with the unit cell shapes.

The investigation of the multiple molecules was facilitated by the recent development of `fromage`,[13,14] a Python library dedicated to studying excited state molecular aggregates and crystals. This work showcases the robustness of its features by applying geometry analysis tools, excitonic coupling evaluation, and ONIOM methods to the crystals.
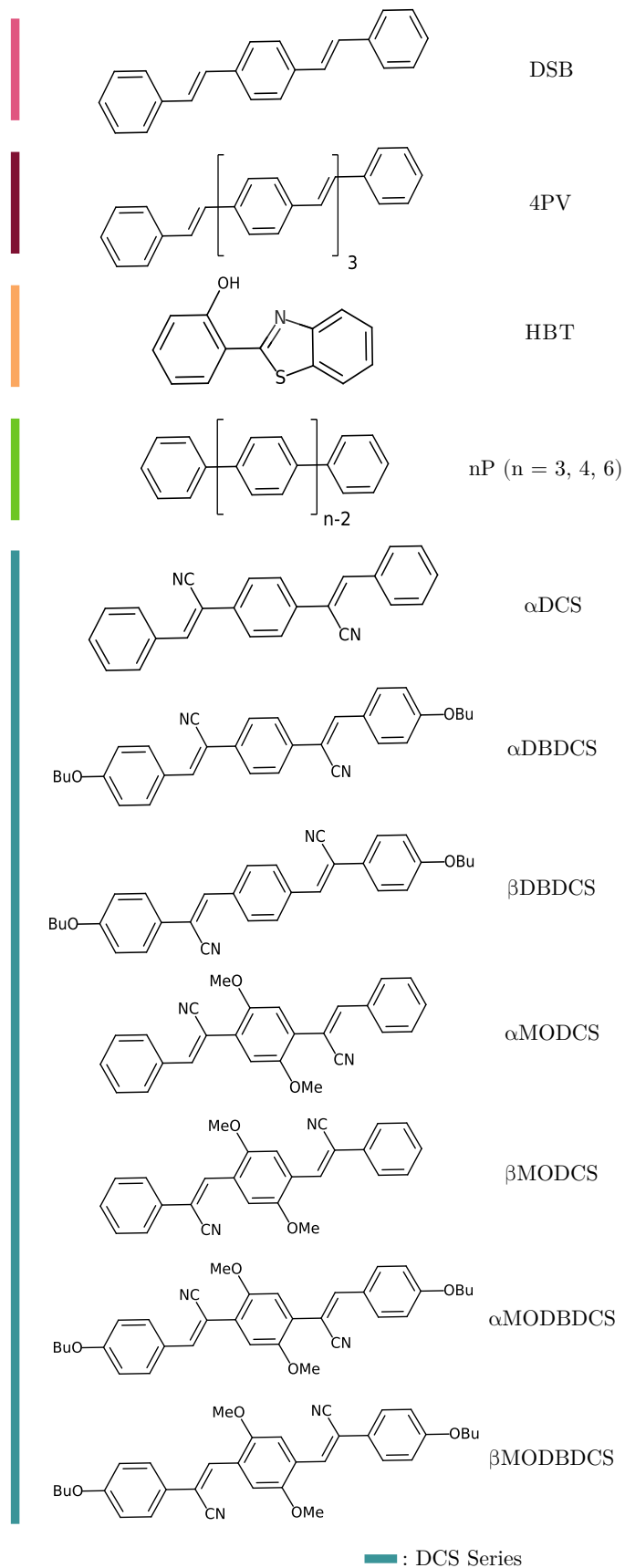
Figure 1 Molecular structures of the studied systems. The colours are carried over in the following figures.

In order to isolate dimers from the lattice, a spherical molecular cluster was extracted from the crystal, and its pairs of molecules with with intermolecular contacts smaller than 4 Å were selected. Then, the intermolecular atomic distances of each dimer were evaluated and sorted so as to provide a fingerprint for the dimer configuration. These distances were finally compared between dimers and if their RMSD fell below 10^{-4} Å, the dimers were considered identical and only one was preserved.

To characterise the configurations of the unique dimers, an orthonormal pair of principal and secondary axes was calculated for each constituent fragment, and the angles between same axes of two molecules was evaluated. To obtain the vectors, first, all atoms of the molecule were projected onto an averaged plane via singular value decomposition. The principal axis was defined as the vector tracing the longest interatomic distance and the secondary axis its perpendicular vector on the averaged plane.[14] This process is represented for a dimer of the 3P crystal in Figure 2.
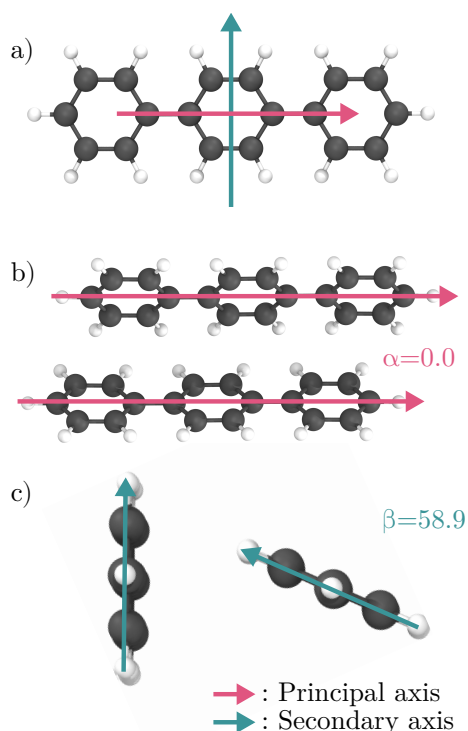

Figure 2 a) Principal and secondary axes on the 3P monomer b) Top view of a 3P dimer c) Side view of the same dimer.

All molecules have rotational symmetry about both of the axes when defined this way apart from HBT which has an inherent orientation. In the case of this molecule, we employed the scheme described in Reference 14 where, by exploiting the two longest interatomic distances on the averaged plane, a set of axes could be defined with consistent orientation.

To evaluate exciton couplings between dimers, the diabatisation scheme by Troisi and Aragó[3], as implemented in `fromage`. The transition dipole moments of the isolated monomers were compared to those in the dimer to construct a diabatic Hamiltonian, whose off-diagonal elements are the exciton couplings. The original algorithm is thoroughly described in the Supporting Information of Reference 3 and in reference 14. The transition dipole moments were calculated TD-ωB97X-D/6-31G(d) method using `Gaussian`.[15] For all systems investigated here, the S_1 and S_2 states from the dimers originated from the linear combination of states from the monomers and were considered for the calculation of the exciton couplings.

For the QM:QM' calculations, on HBT, α-DCS and the nP series, the ONIOM scheme with electrostatic embedding was used. The excited state level of theory (QM) was TDDFT ωB97X-D/6-31G(d), with `Gaussian`, or ADC(2)/SV(P), with `Turbomole`.[16] The high level region was embedded in point charges from RESP calculations of DFT ωB97X-D/6-31G(d) calculated in `Gaussian`. For the polar molecules HBT and α-DCS, the electrostatic embedding was extended to include long range Coulomb interactions using the ONIOM Ewald Embedded Cluster method (OEEC).[13] The ground state level of theory (QM') was DFTB, with `DFTB+` program,[17] and the embedding for the central region was done using RESP charges obtained with the PBE/6-31G(d) method. Conical intersections were located using the penalty function method of Levine and Martinez, to avoid the need for nonadiabatic couplings.[18] Multireference SA-2-CASSCF and MS-2-CASPT2 calculations were performed with Molcas using the 6-31G(d) basis set.[19] The active spaces are reported in the Supplementary Information.

To examine the effect of vibrations on the exciton couplings, the QM:QM' calculations were carried out on dimers. Then, a normal modes calculation was carried out, from which a Wigner distribution of 200 sample geometries were extracted using `Newton-X`.[20,21] The exciton couplings were then evaluated using the diabatisation method.

The Huang-Rhys factors (S_i) for relaxation within the S_1 state, between S_0 and S_1 minima, were evaluated for the members of nP and DCS series in vacuum and crystal environment using the `DUSHIN` code.[22] The computations were based on the normal modes computed at the optimised S_0 and S_1 geometries in vacuum at the (TD-)ωB97XD/6-31G(d) level and in crystal at the QM:QM' level described above. Reorganisation energies (λ_i) decomposed into normal mode contributions are related to Huang-Rhys factors as follows:

$$\lambda_i = \hbar\omega_i S_i \tag{1}$$

The Einstein[20] and Strickler-Berg[23] (SB) relations were employed to evaluate radiative rates and lifetimes of selected fluorophores in solution and crystal. According to Einstein equation for spontaneous decay, fluorescence rate (k_r) with emission energy (ΔE) and oscillator strength (f) can be evaluated as

$$k_r = \frac{2\Delta E^2 f}{c^3} \tag{2}$$

Where all variables and constants are represented in atomic units.

The SB relation takes into account transitions between vibronic wave functions of excited and ground states.[23] According to the SB relation, the radiative rate can be evaluated as[5]

$$k_r = 0.667[\text{cm}^2 \times s^{-1}]\frac{v_F^3}{v_A}n^2 f \tag{3}$$

Where v_F and v_A are vertical emission and absorption energies (in cm^{-1}), f is the oscillator strength, and n is the refractive index of a solvent.

To evaluate exciton hopping rates, the Marcus scheme was employed:

$$v_{ij} = \frac{J_{ij}^2}{\hbar} \sqrt{\frac{\pi}{\lambda k_{\mathrm{B}} T}} \exp\left[-\frac{\lambda}{4 k_{\mathrm{B}} T} \right] \tag{4}$$

Where J_{ij} is the exciton coupling between excited monomers, $\hbar$ is the reduced Planck's constant, k_{B} is Boltzmann's constant, λ is the reorganisation energy computed considering S_1 and S_0, and T is room temperature of 298 K.[24,25]

3 Results and Discussion

3.1 Packing Motifs

Due to the non-covalent nature of molecular crystals, photophenomena often occur locally[3] and can be understood on the scale of the nearest neighbour molecules. When examining conical intersections in the solid state, we are therefore interested in characterising the restrictions on the PES of the central molecule imposed by the immediate environment. The conformational features of the dimer arrangements in the crystal can provide a fingerprint for this crystal packing. Moreover, if the excited state process is not fully localised on one molecule, dimer conformations will be essential in elucidating excited state pairwise interactions.

Figure 3 Illustration of two archetypal packing motifs in molecular crystals.

The packing motifs of these materials are diverse and smoothly varying, making them challenging to classify, however, certain patterns have been identified to occur frequently, and we use these as reference points.[26,27] In particular, herringbone crystals pack in an alternating edge-to-face arrangement, while sheet-like crystals have all molecules sharing

the same orientation arranged in regular layers. These two motifs are represented in Figure 3. For the sake of clarity, in this paper, we employ the terms like *herringbone* and *sheet-like* to refer to the overall crystal packing, and ones like *edge-to-face* or *face-to-face* to denote specific dimer arrangements.

Table 1 Photoactive molecular crystals considered. Φ_f: fluorescence quantum yield in crystal, V_i: steric volume index. [a] Largest dimeric exciton coupling in the crystal, [b] herringbone (HB), sheet-like (S) or other (-), [c] fraction of H (not J) dimers in the crystal, [d] tetrahydro-2-metehylfuran solvent, [e] cyclohexane solvent, [f] chloroform solvent, [g] powder, [h] film.

Crystal	Series	V_i	J (meV)[a]	Packing[b]	H dimer %[c]	Calculated absorption Monomer	Dimer S_1	Dimer S_2	Exp. absorption	Φ_f
DSB	-	1.41	131	HB	100	3.60	3.47	3.65	3.48[d 5]	0.78
4PV	-	1.42	103	HB	100	3.10	2.98	3.19	-	-
HBT	-	1.43	36	HB	83	3.98	3.94	4.00	3.65[e 28]	0.77[g 29]
α-DCS	DCS	1.41	97	S	100	3.74	3.60	3.80	3.61[f 5]	0.90
α-DBDCS	DCS	1.49	53	S	100	3.33	3.19	3.30	3.34[f 5]	0.62
β-DBDCS	DCS	1.53	113	S	100	3.30	3.17	3.34	3.19[f 5]	0.84
α-MODCS	DCS	1.42	32	-	50	3.66	3.64	3.69	3.45[e 5]	0.66
β-MODCS	DCS	1.39	140	S	100	3.06	2.86	3.13	2.95 3.60[f 5]	0.73
α-MODBDCS	DCS	1.44	103	S	100	3.27	3.22	3.29	3.43 3.84[f 5]	0.42
β-MODBDCS	DCS	1.43	121	S	100	2.80	2.68	2.84	2.87 3.40[f 5]	0.46
3P	nP	1.37	98	HB	100	4.36	4.24	4.43	4.51[d 30]	0.67[31]
4P	nP	1.39	99	HB	100	4.16	4.05	4.23	4.13[d 30]	-
6P	nP	2.27	95	HB	100	3.75	3.63	3.82	-	0.30[h 32]

Table 1 summarises the principal data relating to the packing and emission of all systems. For the H/J classification, we consider the values of the oscillator oscillator strengths of the dimers. We immediately note the prevalence of H dimers, accompanied with significant QEF values in contrast with the predictions of Kasha's exciton model.[33] The intermolecular processes in these materials therefore must go beyond point-dipole approximations or be slight enough to not significantly impact the QEF, or both. We also note the prevalence of herringbone and sheet-like crystals, which seem to be highly favoured in these conjugated molecules as efficient packing motifs for aromatic molecules with a mostly planar equilibrium geometry.

The significant dimers of the crystals in consideration were processed in `fromage` to extract their characteristic angles, which were plotted in Figure 4. The DCS series primarily forms sheets, while the other crystals have a clear bias towards herringbone motifs. This is

reflected in the absence of DCS dimers with large secondary angles, where the most angled one is an α-DCS dimer with 24.9°. In contrast, all of the herringbone crystals have dimers both with low and high secondary angles (at least 58.0°). We observe that the secondary axis alone is a robust indicator of the packing pattern, removing the need for individual inspection of the unit cells.
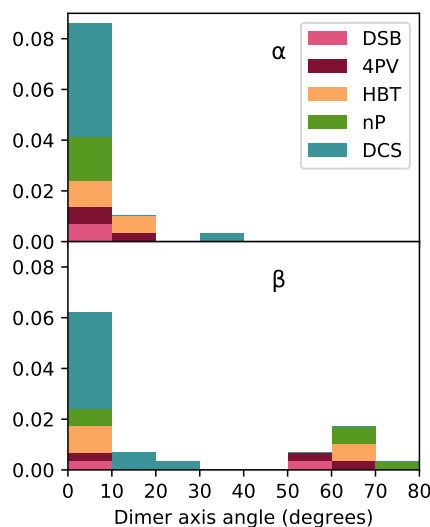

Figure 4 Histogram of the dimeric arrangements in all crystal series. α and β angles correspond to the angles between primary and secondary axes.

The principal axis angles in face-to-face dimers of sheet-like crystals are almost always 0° due to the translational symmetry between layers. Herringbone crystals usually also have parallel principal axes, with some slight deviation due to one 4PV dimer and two HBT dimers. This slight departure from ideal herringbone packing is known in 4PV,[34] where the unit cell includes six molecules instead of two. HBT displays slightly misaligned head-to-tail dimers indicating that each layer of the material in the principal axis direction has an alternating orientation. The notable exception to the nearly parallel principal axes is α-MODCS, with 38.5°, a fingerprint which reflects how it can not be classified as herringbone or sheet-like. A more complete plot of principal versus secondary angles is presented in the Supporting Information, with a focus on the DCS series dimers to highlight the unusual

packing of α-MODCS.

The values of the exciton couplings of the molecules under scrutiny, evaluated at their Frank-Condon region, are a result of structural and chemical features of the dimers formed upon aggregation. We therefore wish to highlight any possible correlations between the packing patterns described above, and the exciton states within the crystal. These states are liable to cause delocalised excitation phenomena, opening avenues for nonradiative decay.

We first examine the dependence of the couplings on the distance between constituent fragments of the dimer. Figure 5 shows the exciton coupling of each dimer of the crystal structures with respect to the centroid-to-centroid distance of said dimer. We observe a clear monotonic downward trend for dimers belonging to every crystal except for HBT. This trend is in line with the limiting behaviour where fragments become non interacting at infinite distances and the coupling should therefore tend to zero. In the middle to long range, the electrostatic interaction between the two fragments approaches a $1/r$ shape where r is the distance between the centers of mass of each electron could. Figure 5 does not have the sufficient resolution to suggest an inverse law as opposed to other monotonically decreasing functions. However, we can observe that dimers from different series have similar exciton coupling given similar centroid-to-centroid distance within a range of 50 meV. This is a surprising result because of the inadequacy of centroid distance as a measure of correlation of neighbouring excited states, ignoring the shape of the molecular wavefunctions altogether.

HBT constitutes a striking exception, where all of the nearest neighbour dimers have exciton coupling values between 20 and 40 meV. In particular, the two closest dimers, with centroid distances close to 5 Å, are about 60 meV below the fit line. The transition densities of these dimers, compared with the monomer transition density are depicted in Supporting Information. The excitation of the isolated molecule is mainly localised in the proton transfer moiety, breaking the apparent symmetry of the two constituent rings. Both closest
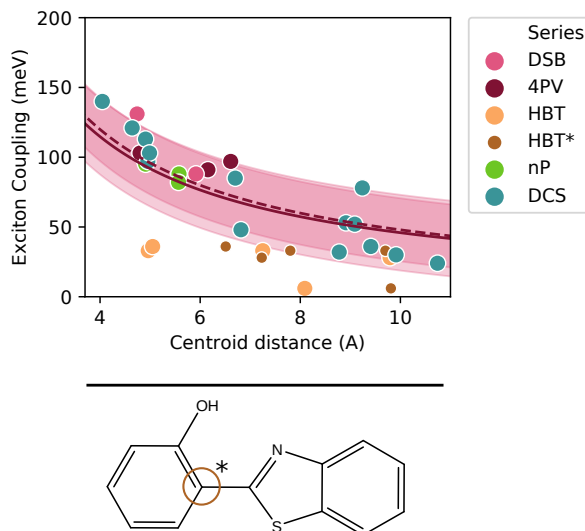
Figure 5 (top) Exciton coupling (J) as a function of the centroid-to-centroid distance of the constituent monomers of each dimer. The values of every dimer are fitted to an inverse law $f(r) = a/r$ *via* least squares. The resulting function, with $a = 459$ is plotted in pink and has a standard deviation of 27, represented by the shaded area. A dashed line represents the same fit but using an aromatic carbon (bottom) as a reference for the distance calculation, denoted HBT*. In this case, $a = 480$ and the standard deviation is 23.

dimer arrangements are aligned in centroid but opposite oriented, effectively distancing the excitation densities. This effect is less pronounced in other molecules because they are all symmetric in orientation of their long axis. By measuring the distance between HBT molecules with an aromatic carbon as a reference point, the exciton coupling values adopt a clearer downward trend, albeit shifted lower than for the other series.

Excluding HBT, the dimers are roughly split into two group, those below 7 Å in separation, with couplings ranging from 82 to 140 meV and those above 7 Å with couplings from 24 to 64 meV. Those in the former group are overall above the a/r trend line, and those of the latter below. This may be explained by the added proportion of exciton coupling resulting from exchange in the strong coupling regime. Ref. 35 found that when Coulombic coupling exceeds 70 meV in organic semiconductor materials and light-harvesting complexes, the exchange portion of the coupling always shares a sign with its electrostatic counterpart, thus increasing the total coupling. This is consistent with the deviation of the limiting behaviour of the total coupling from a Coulombic inverse law.

As a methodological aside, the use of the diabatisation method for calculating exciton coupling provides a good benchmark value. A simpler method is to approximate the exciton coupling as half of the S_2–S_1 energy gap, which is exact in the limit of linear resonant molecules.[36] Due to the strong degree of symmetry characteristic of the herringbone and sheet-like packing, this turns out to be a very good approximation in this sample of crystals. The comparison is provided in the Supporting Information.

We observe that molecules with similar centroid-to-centroid distances but different packing arrangements still have very similar exciton coupling. For instance α-MODBDCS has a dimer with exciton coupling of 103 meV and a centroid-to-centroid distance of 5.0 Å, and 4P has a dimer with a coupling of 101 meV and a distance of 4.9 Å, despite the respective packings being sheet-like and herringbone respectively. This is, of course, not to say that the individual excited state chemistry of each dimer can be reduced to a distance. In fact, it highlights how Kasha's model, where the tilt of the dimers alone determines their exciton coupling, is not robust in these systems.[33]

In the Supporting Information, we continue this discussion, showing how, for the DCS series, the intermolecular conformation has little impact on the exciton coupling values accessible vibrationally. Instead, the geometry of the constituent monomers is the main indicator of broadness, and the centroid distance of absolute value of the exciton coupling within one same series.

3.2 Role of Conical Intersections

As we have demonstrated, the prevalence of herringbone and sheet-like packing patterns in these materials results in transferable geometric and excitonic properties. However, these alone do not explain their photoluminescence properties, namely their QEF in crystal and solute phases. The interconnectedness of intra- and intermolecular factors which mediate their radiative and nonradiative pathways makes the determination of the QEF, even at a qualitative level, a much more system-specific task.

We have previously observed that the accessibility of conical intersections is the determining factor dictating the luminescence of several luminescent laser materials.[8,9] In this section, we assess the efficacy of this lens in explaining the luminescence of systems with diverse properties, case by case. We hope to highlight different consequences of crystallisation on the accessibility of conical intersections, and to what degree they influence the QEF.

To achieve this, we have chosen two SSLE crystals with different crystal packing, and a family of linear molecules where increased chain length corresponds to lower QEF.

HBT

2-(2'-hydroxyphenyl)-benzothiazole (HBT) displays SSLE upon its aggregation to herringbone single crystal[37] and liquid crystal phases.[38] While HBT has negligible QEF in organic solvents, it significantly increases in aggregate phases, amounting to 0.77 in powder samples.[29,39] For this reason, HBT-derivatives are proposed as materials for organic light-emitting diodes (OLEDs) and fluorescent probes.

The underlying excited state relaxation mechanism of HBT-based systems in vacuum and solution includes excited state intramolecular proton transfer (ESIPT).[40,41] The ESIPT is a four-step mechanism enabled by an intramolecular hydrogen bond. It consists of a photoexcitation, excited-state proton transfer, torsional motion, and ground-state proton back-transfer.[40,42] Large reorganisation energies, dependent on solvent nature, are associated with this process.[40,42] A similar mechanism has been proposed in crystal environment.[42,43] Due to the lack of studies that support it, we examine radiative and nonradiative mechanisms in solution and crystal.

Following the S_1 excitation of enol form, two possible pathways exist: relaxation to enol S_1 minimum and/or ESIPT yielding the cis-keto form in the S_1 state. The reorganisation energies obtained from (TD-)ωB97X-D/6-31G(d) computations of enol and cis-keto forms suggest that ESIPT is energetically more favorable in both solution/crystal, releasing 0.38/0.39 eV in comparison to the S_1 enol relaxation which releases 0.28/0.27 eV. Having

reached the S_1 minima in the enol and keto forms, the relaxation to the ground state could proceed *via* radiative and nonradiative processes.

Fluorescence experiments have observed weak emission from both forms in solution,[44] while in crystal (nanowires) intense emission only from cis-keto form (planar and twisted) is observed.[45] Radiative rates evaluated based on Einstein formula indicate that crystallisation increases radiative rate of the enol form for approximately 50 %, whereas it has a minor effect on fluorescence rate of the cis-keto form (Table 2). Since fluorescence is observed only from the latter form, these results imply that SSLE originates in hampering of nonradiative processes, which we here examine in detail.

Table 2 Computed S_1 energies in eV ($E(S_1)$) with corresponding oscillator strength (f), radiative rates calculated with the Einstein relation in ns^{-1} (k_r^{Ein}), reorganisation energies of low-frequency modes in meV (λ_{low}) for enol and cis-keto forms of HBT molecule. The superscripts indicate the medium, where "sol" is cyclohexane solvent and "cr" is crystal.

Molecule	$E(S_1)^{sol}$	f^{sol}	$k_r^{Ein,sol}$	λ_{low}^{sol}	$E(S_1)^{cr}$	f^{cr}	$k_r^{Ein,cr}$	λ_{low}^{cr}
HBT (enol)	3.53	0.66	0.85	7	3.66	0.53	1.27	6
HBT (cis-keto)	2.70	0.32	0.41	55	2.93	0.30	0.35	53

We now attempt to rationalise the SSLE mechanism of HBT *via* the lens of the Restricted Access to Conical Intersections (RACI) model outlined by Blancafort *et al.* in References 6 and 7. This framework compares the energy of the MECI energy to the vertical absorption in order to determine the viability of internal conversion through a conical intersection. Our previous work has already proven the efficacy of this method for ESIPT molecules, which indicates that other nonradiative mechanisms can be put aside for now.[8,9] We used similar ONIOM Ewald Embedded QM:QM' Cluster methods (OEEC), to optimise critical regions of the solid state potential energy surface. We used the Ewald embedding scheme to account for the long-range electrostatic interactions of the material, which can be important in polar crystals. We chose the ωB97X-D functional since it has reproduced accurate ESIPT optimised geometries in the past, and predicts a QM:QM' absorption energy of 4.20 eV, as compared to the experimental value of 3.65 eV. The results are depicted in Figure 6.
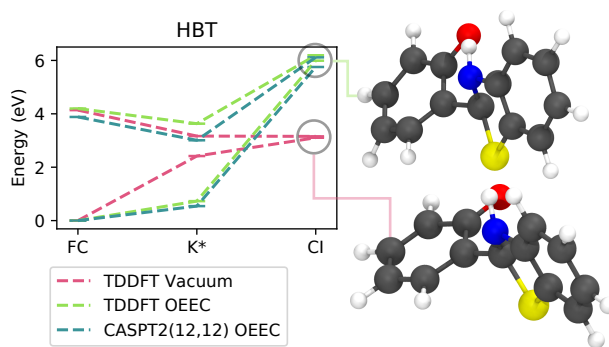
Figure 6 HBT energy at critical points of its excited state potential energy surface. The vacuum calculation used TD-ωB97X-D/6-31G(d) and the crystal calculation TD-ωB97X-D/6-31G(d):DFTB.

Crystallisation has a significant impact on the Stokes shift of HBT. Whilst in vacuum, the difference between absorption and emission energies was 3.39 eV—a huge value, representing 93% of the absorption energy—in crystal this value was red shifted to 1.30 eV. The important Stokes shift in vacuum is due to the ESIPT process in HBT, which changes the chemical character of the molecule in the excited state, producing large geometrical reorganisation. In this case, the reorganisation is hindered within the crystal environment.

The conical intersection which involves only a rotation of the oxygenated aryl bond is the S_1–S_0 MECI in solution, but becomes very unstable due to the steric hindrance of the nearest neighbour molecules upon crystallisation. The S_1–S_0 MECI in crystal additionally involves the pyramidalisation of one of the molecular backbone carbons, thus reaching a distorted but spatially compatible geometry within the close packed environment. However due to this distortion, the crystal MECI remains unstable, surpassing the absorption energy by 1.9 eV. If we use MS-2-CASPT2(12,12)/aug-cc-pVDZ as the excited state method instead, using the geometries optimised in TDDFT, the results are similar, with an absorption of 3.88 eV—now only 0.23 eV above the experimental value—and a MECI 2.05 eV above absorption. In this case, the S_1–S_0 gap at the MECI geometry is 0.36 eV. Further scanning of the CASPT2 PES would help narrow this gap, but would be unlikely to reduce the energy by up to 2.05 eV.

Upon crystallisation, the S_1–S_0 MECI becomes inaccessible for a molecule excited at

17

FC point. This blocks the principal nonradiative decay channel, and explains the rise in QEF from measurements in organic solvent and in powder samples. In this case, alternative nonradiative decay channels are not important enough in the crystal to prevent the formidable 0.77 efficiency.

The destabilisation of the conical intersection upon crystallisation in this material parallels the important lowering of the Stokes shift. Indeed, they are both results of a flexible molecule accessing highly distorted regions of its PES in the excited state, which are then blocked by the immediate environment. Indeed the rotational flexibility of the molecule is along its principal axis, which has a forbidden region in herringbone crystals between 10° to 50° as shown in Figure 4. Therefore we can postulate the herringbone packing combined with flexibility along the primary axis and the large vacuum Stokes shift as indicators of a possible RACI mechanism in other crystals.

This hindrance due to the herringbone packing is depicted in Figure 7 a). Note that the packing in HBT differs from the other herringbone-packed crystal—3P—in the inclusion of a very close face-to-face neighbour. However the determining feature of herringbone packing in this study is the other, edge-to-face dimer, which imposes less restriction on the secondary axis rotation degree of freedom.
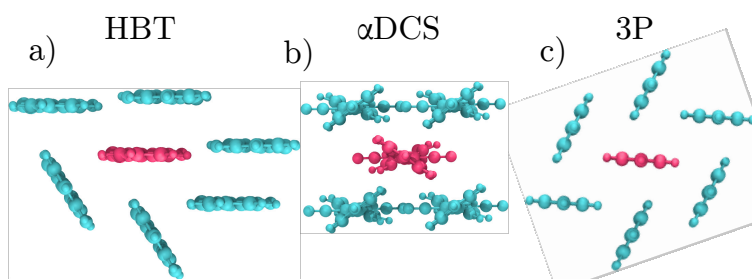

Figure 7 Packing structures of a) HBT, b)α-DCS, and c) 3P. Each molecular cluster is depicted along the principal axis direction, with the central molecule in pink and the nearest neighbours in blue. In and out of plane nearest neighbours have been removed for clarity of viewing.

We also consider the internal conversion process on the grounds of the RIM model. We computed reorganisation energies for relaxation within S_1 state resolved into normal mode contributions in solution and crystal, based on (TD-)ωB97X-D/6-31G(d) normal modes of

S_0 and S_1 states (Table 2) Reorganisation energy corresponding to the torsional mode activated to reach the S_1–S_0 MECI is negligible and, contrary to expectations, the reorganisation energies of low-frequency modes are not significantly hampered in aggregate phase. This is a consequence of the harmonic representation of S_0 and S_1 potentials employed in computation of reorganisation energies, which cannot predict the S_1–S_0 crossing at high activations of torsional mode, where the PESs are affected by anharmonicity.

Crystal environment can decrease radiative response *via* photon reabsorption and intermolecular processes, such as exciton hopping. The effect of photon reabsorption is minimised in HBT crystal due to a significant Stokes shift between excitation of absorbing enol (3.66 eV) and emission of cis-keto form (2.93 eV) (Table 2). Due to relatively small exciton coupling (0.036 eV) in comparison with reorganisation energies for relaxation within S_1 states (0.28 eV for enol form), exciton hopping is expected to be a slower process compared to intramolecular relaxation.

DCS Series

Now, we investigate the excited state decay channel of another aromatic molecule with a different structured backbone, based on the DSB molecule. α-DCS is a DSB derivative displaying in impressive rise of QEF from 0.002 to 0.90 from solution to single crystal.[5]

Its geometry was optimised in chloroform solvent using PCM to find its ground and excited state minima and conical intersection geometry. The results are shown on Figure 8. The absorption energy was 3.84 eV, in close agreement with the experimental value of 3.80 eV. The FC minimum was characterised by a tilt of the inner ring with respect to the outer rings of 67.2°, whereas the S_1 optimisation led to a more planar geometry with an angle of 21.3°. This large reorganisation led to an emission energy of 2.84 eV, shifted 1.01 eV away from the absorption energy. In vacuum, this Stokes shift was found to be 0.80 eV, 20% of the absorption energy.

The moderate difference between absorption and emission energy is enough to discourage reabsorption, but is not on the scale of HBT. Furthermore α-DCS packs in a sheet-like

pattern, not a herringbone one, further distancing the two cases. We would like to ascertain whether the elevated vacuum Stokes shift and the herringbone packing pattern are required to observe a RACI mechanism in these luminescent materials.
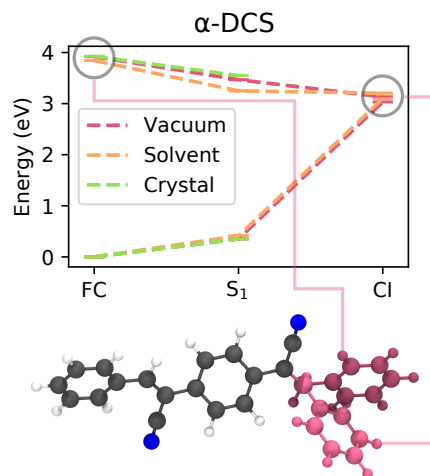

Figure 8 α-DCS energy at critical points of its excited state potential energy surface. The vacuum and solvent calculation used TD-ωB97X-D/6-31G(d) and the crystal calculation TD-ωB97X-D/6-31G(d):DFTB.

The molecule was reoptimised in its crystal phase using OEEC. Here, the FC geometry had a tilt of 62.9° but the planarisation of S_1 was significantly hindered, only reaching 47.1°. We observe that the crystal packing reduces the flexibility of the molecule, which is calculated to absorb at 3.93 eV and emit at 3.20 eV, producing a Stokes shift of 0.73, a value smaller than in solution by 0.3 eV and smaller than in vacuum by 0.07 eV. This case contrasts with HBT, where crystallisation favoured more planar arrangements of the molecule. The sheet-like packing in the α-DCS crystal energetically encourages excited molecules to remain in their packing geometry due to the symmetrical steric hindrance of neighbouring face-to-face units on either side of the excitation. This packing is represented in Figure 7 b). The consequence for α-DCS, is that since the ground state molecules have a central ring deviated from the averaged plane, excited molecules will deviate less from this configuration.

The increased rigidity of the environment also has implications for the geometry of the S_1–S_0 MECI. The access to the conical intersection geometry in solvent for similar

molecules has been characterised by a rotation about a double bond of the backbone, causing one ring to be on a perpendicular plane from the other two, and a pyramidalisation of the carbon connecting the rotated ring to the backbone.[46] We located a similar conical intersection for α-DCS, where the rotation was of 88.8° about the same vinylene bond as reported in Reference 46, but involving no pyramidalisation. In either case, the rotation involved in the access to this S_1–S_0 MECI supposes a large reorganisation which represent a quenched nonradiative decay channel in solution, and a blocked one in crystal. Indeed the crystal packing is too dense to allow for the backbone to draw an arc of nearly a right angle, which would distort the molecule by rotatation along both in its primary and secondary axis directions. Instead the penalty function MECI optimisation algorithm pursues a double bond stretching CI too distorted to evaluate even with multireference methods.

Other emissive DSB-based molecules have similar molecular backbones and packing, as shown in Figure 4, pointing to a similar quenching of the internal conversion decay pathway. They have been investigated in a series of studies for their promising SSL properties.[5,46,47] They all have cyano-group (CN) substituents on the vinylene units which connect their phenylene rings. DBDCS and MODBDCS have additionally buthoxy-groups (OBu) on lateral phenylene rings at their para positions. Apart from CN- and OBu-substituents, the MODBDCS molecules are distinguished by methoxy-groups (OMe) on central phenylene rings in their meta positions. MODCS is characterised by OMe-substitutions on central phenylene rings. α- and β-members of the series differ from each other by positions of CN- groups on vinylene units with respect to the phenylene rings; the former having CN- groups closer to the central ring, and the latter closer to lateral phenylene rings.

All members of the series are emissive in the crystal form, with higher efficiency than in solution. In particular, the α- systems are completely non-emissive in solution. As noted in the previous sections, changes in QEF are understood as a competing change in radiative and non-radiative rates, with the latter being contributed to by differing vibra-

21

Table 3 Experimental radiative rates in ns^{-1} (k_r), nonradiative rates in ns^{-1} (k_{nr}), luminescent efficiency (Φ_f), and computed reorganisation energies for vibrational modes of less than 0.031 eV (250 cm^{-1}) in meV (λ_{low}) for the DCS series. The superscripts indicate the medium, where "sol" is chloroform solvent, "vac" is vacuum, and "cr" is single crystal

Molecule	$k_r^{\text{sol}\,5}$	$k_{nr}^{\text{sol}\,5}$	$\Phi_f^{\text{sol}\,5}$	$\lambda_{\text{low}}^{\text{vac}}$	$k_r^{\text{cr}\,5}$	$k_{nr}^{\text{cr}\,5}$	$\Phi_f^{\text{cr}\,5}$	$\lambda_{\text{low}}^{\text{cr}}$
α-DCS	0.35	175	0.002	95	0.43	0.05	0.90	46
α-DBDCS	0.5	250	0.002	88	0.05	0.02	0.70	16
β-DBDCS	0.45	0.39	0.54	90	0.14	0.03	0.84	35
α-MODCS	0.11	5.4	0.02	94	0.19	0.1	0.66	54
β-MODCS	0.15	0.60	0.2	89	0.04	0.02	0.73	31
α-MODBDCS	0.23	77	0.003	59	0.09	0.12	0.42	9
β-MODBDCS	0.22	0.50	0.31	77	0.02	0.02	0.46	9

tional wavefunction overlap, intermolecular excitonic processes, and conical intersection accessibilities.

The nonradiative rates only increase upon aggregation for α-DCS and α-MODCS, as is reported in in Table 3.[5] Therefore, we can expect an important restriction of nonradiative decay mechanisms upon crystallisation for the series.

Within the RIM model, the reduction in nonradiative decay rate upon crystallisation would come from the quenching of low energy vibrational modes. As is shown in Table 3 these modes are indeed reduced in the crystal phase for the DCS series. However, no clear trends emerge linking the quenching of vibrational modes upon crystallisation to the change in QEF of the systems, though they cannot be excluded as a contributing factor to the enhanced emission.

To probe for excitonic dissipation, we can focus on the case of the strongest coupled system, β-MODCS, as seen on Table 1, with an exciton coupling of 140 meV. This does not impede a very efficient emission of 0.73, despite its low radiative rate reported in Table 3. As shown in Figure 4, most crystals share the characteristic face-to-face dimer packing of sheet-like crystals, indicating that the character of their excitonic states should not be radically different. The principal exceptions are α-DCS and α-MODCS, where the former still

displays the greatest crystal luminescent efficiency of the series, and the latter a mere 32 meV of exciton coupling. We can conclude that within this series, due to the magnitude of the reorganisation energies (Table S2), excitonic states do not produce efficient transport which would lead to dissipation of the excited state.

As for the access to conical intersections, there is reported evidence for is importance in the series. Reference 47 observes a a rise in nonradiative decay rates with increasing FC energy in solution. This indicates the comparatively low importance of vibrational decay in the nonradiative rate of this family, due to a lesser overlap between ground and excited state vibrational wavefunctions in the low nonadiabatic coupling regime; leaving the RACI mechanism such as the one previously outlined for α-DCS as the principal cause of SLE.[48]

The dominance of conical intersection decay in this series can also be linked to the low but present strength of the β- molecules in solution. The position of the CN- substituents upon the rotating section of the double bond which drives the access to the conical intersection, at least in α-DCS, can constitute a hindrance to the the motion.

Moreover, the RACI model depends on the rigidity of the molecules in the excited state, where a smaller conformational freedom of the molecule results in fewer pathways to the conical intersection to restrict. This is consistent with the overall greatest QEF, attributed to the smallest molecule—α-DCS, with 0.90—and the lowest QEF to the ones with the most substituent—α-MODBDCS and β-MODBDCS, with 0.42 and 0.46 respectively. It is, however, noteworthy that α-MODBDCS and β-MODBDCS have the smallest reorganisation energies within the series (0.49 and 0.46 eV).

We can observe from the behaviour of the DCS series that sheet-like packing has similar strictive consequences on the accessibility of conical intersections than in the herringbone-packed HBT. The face-to-face dimer arrangement imposes a strong restriction of motion for rotations along both the principal and secondary axes. Since the conical intersection for α-DCS is mediated by the rotation about the centre of a vinylene bond, this type of reorganisation is forbidden twofold by the sheet-like packing.

*n***P**

Finally, we compare our findings related to SSLE systems to the photochemistry of a luminescent family of crystals which also emit as a solution.

p-Hexaphenylene (6P) has been employed as a building block of photonic nanofibers,[49,50] and as a material for nanolasers,[51,52] exploiting its amplified spontaneous emission,[53] thanks to its fluorescence and structural characteristics favourable for growing well-defined molecular architectures.

6P has an experimental fluorescence quantum yield of 0.85 in solution and 0.30 in crystal,[32] whereas the much smaller 3P has a yield of 0.82 in solution[54] and 0.67 in crystal.[31] We would like to rationalise this difference, also considering the intermediate case of 4P. In contrast with HBT and α-DCS, these systems are emissive in vacuum, meaning that their excited state process in vacuum is not dominated by nonradiative deactivation.

We optimised the structures of the emitting $\pi\pi^*$ states of 3P, 4P, and 6P, applying TD-ωB97X-D in cyclohexane solvent using PCM and in the crystal phase with the QM/QM' cluster method at the TD-ωB97X-D/DFTB level. The computed S_1 energies and oscillator strengths are reported in Table 4. We can extract several interesting trends.

Table 4 Computed S_1 energies in eV ($E(S_1)$) with corresponding oscillator strength (f), radiative rates calculated with the Einstein relation and SB formula in ns^{-1} (k_r^{Ein}, k_r^{SB}), experimental luminescent efficiency (Φ_f), and reorganisation energies in meV (λ) for the *n*P series. λ_{tot}^{cr} includes the reorganisation energies for S_1 and S_0. The superscripts indicate the medium, where "sol" is cyclohexane solvent, "vac" is vacuum, and "cr" is crystal. [a]Powder samples. [b] Single crystal.

Molecule	$E(S_1)^{\mathrm{sol}}$	f^{sol}	$k_r^{\mathrm{Ein,sol}}$	$k_r^{\mathrm{SB,sol}}$	Φ_f^{sol}	λ^{vac}	$E(S_1)^{\mathrm{cr}}$	f^{cr}	k_r^{cr}	Φ_f^{cr}	λ^{cr}	$\lambda_{\mathrm{tot}}^{\mathrm{cr}}$
3P	3.69	1.37	0.81	1.24	0.82[54]	510	3.83	1.19	0.76	0.80^{a}[31] , 0.67^{b}[31]	350	690
4P	3.49	1.91	1.01	1.54	-	540	3.62	1.74	0.99	-	370	710
6P	3.32	2.81	1.35	2.17	-	490	3.34	2.86	1.38	0.30^{b}	290	430

As the length of the chain increases from three to four and four to six, the emission energy decreases. The trend is similar in solution and in crystal where in the former, the emission energy decreases by 0.20 eV from 3P to 4P and by 0.17 eV from 4P to 6P, and in the latter the differences are 0.21 eV and 0.28 eV.

We can relate this phenomenon to the degree of delocalisation of the transition density in the different molecular structures. In the case of 3P, the S_1–S_0 transition density is mostly localised on the central phenyl ring and surrounding C–C bonds, while in the case of 4P and 6P, it is localised on two central phenyl rings and surrounding C–C bonds. The transition densities are depicted in the Supporting Information. This delocalisation destabilises the HOMO and stabilises the LUMO, which contributes to narrowing the S_1–S_0 energy gap. This could also explain the increases in oscillator strength by 0.54 and 0.90 in solution, and 0.55 and 1.12 in crystal, where a more diffuse transition is correlated with a greater overlap between initial and final wavefunctions and a greater transition dipole moment.

In comparison with the solution, the crystal environment raises the emission energy by 0.1 eV and lowers the oscillator strength by 0.2 for 3P and 4P. These effects are, however, negligible for 6P.

The emission rates, k_r, computed applying Einstein relation in solution and crystal and applying the SB relation in solution, increase with backbone length. This is due to the large increase of oscillator strength relative to the decrease in emission energy. The k_r values in solution and in crystal are very similar throughout the series due to competing effects of crystallisation increasing the emission energy and decreasing the oscillator strength for 3P and 4P.

The rates in solution obtained based on the SB relation are about twice as large as the values obtained from Einstein relation. This is due to the transitions between vibronic wave functions of the excited and ground states, which the Einstein relation neglects.

The decrease in QEF of 6P with respect to 3P is not explained by the behaviour of radiative rates which instead increase with chain length. This indicates the importance of nonradiative relaxation pathways in this series, despite the fact that it emits efficiently in solution and crystal. We first examine a rationalisation based on conical intersections, as this was a determining factor for HBT and α-DCS.

The S_1–S_0 minimum energy crossing points were optimised at the ADC(2)/def-SV(P) level in vacuum and crystal for 3P, 4P, and 6P. TD-ωB97X-D/6-31G(d) was also attempted but electronic convergence problems arose due to the highly distorted conformations involved. Previous studies indicate that ADC(2) can represent accurate S_1–S_0 crossing topologies in organic chromophores despite being a single reference method.[55]

The optimised vacuum S_1–S_0 MECI geometries of 3P and 4P, represented in Figure 9, correspond to ring puckering conical intersections with puckered phenyl rings on which the S_1 transition densities are localised.

The central phenyl ring at the MECI geometry of 3P in vacuum is a prefulvene kind of conical intersection,[56] characterised by a half-boat structure with the C_s symmetry. The puckering of the central ring is accompanied by flapping motion of peripheral phenyl rings, resulting in a highly distorted structure with one phenyl ring roughly perpendicular to the puckered ring. Similarly, the S_1–S_0 MECI structure of 4P in vacuum corresponds to a puckered half-boat structure of one of the central rings, while the other one, on which transition density is also localised at the S_1 minimum, displays slight out-of-plane distortion.

However, in the crystal, flapping motions are partially hindered due to the tight packing. The flapping distortion in particular represents a rotation along the secondary axis of the molecule, which is moderately hindered by the steric hindrance of the edge-to-face nearest neighbours, characteristic of herringbone packing depicted in Figure 7 c). The crystal S_1–S_0 MECI geometries have a different identity, featuring a pronounced puckering of one C atom of the central ring and substantial out-of-plane distortion of H atom attached to it. The rest of the molecule remains in plane. This type of conical intersection corresponds to another point at the prefulvene CI seam.

For both 3P and 4P, as shown in Figure 9, the optimised MECI geometries lie above the S_1 excitations at the FC point, both in vacuum and crystal, implying that this kind of internal conversion is inefficient for these systems. The energy of the 3P vacuum conical intersection, obtained with CASPT2(10,10)/6-31G(d)//CASSCF(10,10)/6-31G(d), lies
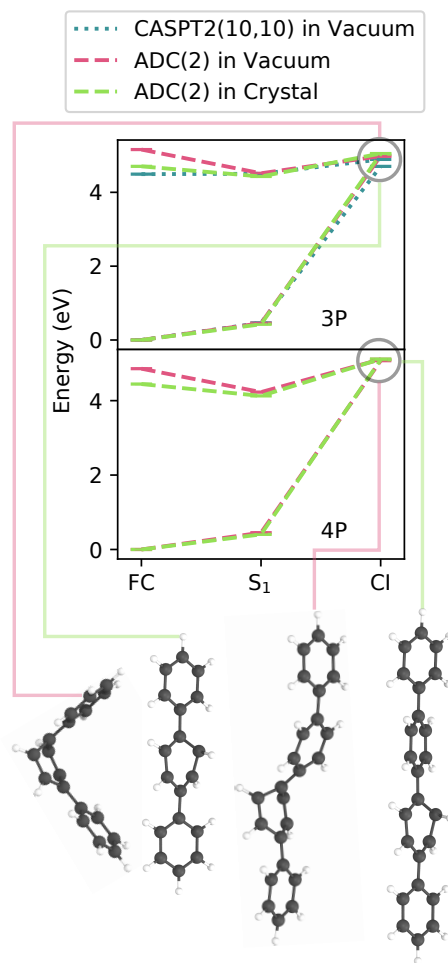
Figure 9 Energies of S_0 and S_1 states of 3P and 4P at the FC point, S_1 minima, and S_1–S_0 MECI in vacuum (left) and crystal (right) computed at the RI-ADC(2)/def-SV(P) level. For the comparison, in the case of 3P, the corresponding CASPT2(10,10)/6-31G(d)//CASSCF(10,10)/6-31G(d) and CASPT2(8,8)/6-31G(d)//CASSCF(8,8)/6-31G(d) results are given.

0.30 eV above the S_1 excitation at the FC point. ADC(2) successfully describes the region of the conical intersection of 3P and predicts the MECI energy close to the value obtained with CASPT2(10,10)/6-31G(d)//CASSCF(10,10)/6-31G(d), but it overestimates the vertical excitation at the FC region. In the case of 4P, the vacuum MECI optimised at the ADC(2)/def-SV(P) level is 0.24 eV above the S_1 state at the FC region. For both systems, the optimised MECI structure in crystal is more energetic compared to the one in vacuum, as has been the trend for HBT and α-DCS. The MECIs of 3P and 4P lie 0.34 eV and 0.67 eV above the excitation in the FC region, based on the ADC(2)/def-SV(P) optimisations.

Unlike for HBT and α-DCS, the nP series conical intersections in solution involve puckering, a highly energetic conformation. This explains their inaccessibility, which blocks this kind of nonradiative decay in solution. For HBT, there is an energy change of 3.0 eV between the vacuum and crystal conical intersection geometries, whereas for 3P and 4P the shift is less than 0.1 eV. We can conclude that in this case, already puckered conical intersections do not become significantly more inaccessible upon crystallisation.

The ADC(2)/def-SV(P) optimised MECI of 6P in vacuum corresponds to a puckering conical intersection with a prefulvene-like structure of the central ring. The rest of the chain is highly distorted due to rotation of terminal phenyl rings, as shown in Figure 10.
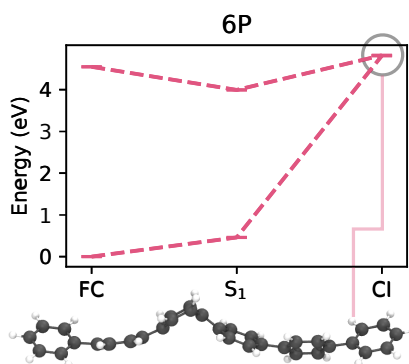

Figure 10 Energies of S_0 and S_1 states of 6P at the FC point, S_1 minima, and S_1–S_0 MECI in vacuum computed at the RI-ADC(2)/def-SV(P) level. The MECI structure is represented in the bottom.

The S_1 state at the optimised vacuum S_1–S_0 MECI is 0.18 eV above the vertical excita-

tion at the FC point, implying that this is an unfavourable nonradiative decay pathway, as shown in Figure 10. The conical intersection optimisation in the crystal could only minimise the S_1–S_0 gap to 0.3 eV, with an energy inversion between S_1 and S_0. This shows the inadequacy of single reference methods to characterise conical intersections in the case of 6P, which is also too large for computationally affordable and accurate multireference methods. However, multireference methods confirmed the accuracy of ADC(2) for 3P, so if we assume this to apply to 6P, then we observe a MECI energy several eV above the FC energy, making it inaccessible.

Conical intersections are therefore rightly found to be at least partially inaccessible for 3P and 4P, blocking this nonradiative decay channel. However this barrier is even higher in 6P, which has lower QEF than 3P, indicating the importance of alternative nonradiative decay mechanisms for this crystal.

Another explanation for the increased nonradiative decay rate of 6P due to internal conversion would be a vibrational nonradiative mechanism. This would be consistent with the lower S_1 energy of 6P, thus enabling large vibrational wavefunction overlap. However, the low vibrational reorganisation energies of 3P and 6P are of the same order in solution and in crystal. Crystallisation reduces these energies to 10% for both systems, as is reported in the Supporting Information, which does not significantly impact the emissivity of 3P, and should therefore not have a different impact on 6P.

Stampfl *et al.* proposed that the decrease of quantum efficiency upon aggregation in 6P is induced by intermolecular excitonic phenomena.[32] This conclusion is based on a linearly decreasing luminescence efficiency with temperature, instead of an Arrhenius-type dependence. The former is explained by increased excitonic collision probabilities on higher temperatures, whereas the latter would be associated with intramolecular vibrational radiationless deactivation.

Exciton hopping rates are quadratically dependent on the exciton coupling within a crystal, and inverse exponentially dependent on the reorganisation energy, as shown in

Equation 4. The exciton coupling in 6P crystals of 95 meV reported in Table 1 is of the same order as for 3P, with 98 meV. In contrast, the total reorganisation energy of 6P in crystal is 0.43 eV, compared to 3P's 0.69 eV. This difference results in a hopping rate 15.0 times greater in 6P than in 3P, which allows for nonradiative excitonic processes leading to the reduced QEF in 6P.

In summary, vibrational and nonadiabatic nonradiative decay channels are mostly blocked in both vacuum and crystal for all members of the nP series. The drop in QEF of 6P upon crystallisation is due to its particular property of displaying strong exciton coupling, whilst having a low reorganisation energy compared to 3P.

4   Conclusions

In this article, we have reviewed the crystalline excited state properties of thirteen organic molecular crystals with luminescent behaviour. We used a geometry analysis tool to characterise the different nearest neighbour dimers present in these crystals and associate them to particular crystal packing motifs. We observed that within one series of similar molecules–DSB derivatives–the packing motif determined the centroid-to-centroid distance of the resulting molecules.

This distance was shown to have direct implications as to the value of the exciton coupling between constituent fragments. Chemically different molecules were found to have similar exciton coupling values within a range of 50 meV. The weakness of this model was highlighted in the HBT crystal, where the centroid of the molecules is far away from the area with most electronic reorganisation upon excitation.

We then investigated the internal conversion decay channels for five of the crystals and how they were affected by their crystal environment. For these luminescent materials, the conical intersection energy was systematically found to be higher than the absorption energy, in crystal.

HBT and α-DCS rotation involved in their vacuum or solvent phase conical intersection,

and had a higher energy crystal conical intersection. We found that herringbone packing effectively blocked rotations about the principal axis, whilst sheet-like packing blocked rotations about both the principal and secondary axes. Clear links between the access to the conical intersection and the QEF were drawn, rationalising the SSLE of these crystals by the RACI model. Whilst a high Stokes shift was another indicator of a RACI process, it was not necessary, as exemplified by α-DCS. Vibrational decay was found not to be a strong nonradiative decay channel in either molecule, making them ill-suited to the RIM model.

In the nP series, conical intersections had puckered geometries in vacuum, and found alternate puckering patterns in the crystal with close to equivalent energy profiles. The quenching of emission in 6P with respect to 3P was neither attributed to a more readily accessible conical intersection, nor to vibrational decay channels. Instead, the extensive conjugation of 6P allowed for a low reorganisation energy combined with high exciton coupling. These properties combine to allow efficient exciton transport, which leads to nonradiative decay when the exciton reaches a defect, phase boundary or surface.

Overall, excited state decay mechanisms remain relatively system specific due to the formidable breadth of chemical space. Fluorescence, internal conversion, and excitonic dissipation are competing mechanisms, interlinked by their relation to crystal structure. The complexity of this relationship is exemplified by the diverse luminescent behaviour in solution of the molecules in this study, despite their consistent efficient luminescence in as crystals. Programs like `fromage` prove themselves to be essential in disentangling the holistic mechanisms behind such phenomena.

Our study of conical intersections points to a likely RACI mechanism when the SSLE molecules reach minimal energy conical intersections through rotation in vacuum. Puckered conical intersections are inherently less stable, but do not suffer increased instability in herringbone or sheet-like packing environments, which are prevalent in luminescent organic molecular crystals.

Acknowledgements

Supporting Information Available

The Supporting Information is provided free of charge. It includes geometries, information about the crystal structures, dimer angle densities, the transition densities for HBT, exciton couplings, the description of the CASSCF active space, analysis of the normal modes and reorganization energies and the transition plots for the nP series.

References

(1) Shuai, Z.; Peng, Q. Excited states structure and processes: Understanding organic light-emitting diodes at the molecular level. *Phys. Rep.* **2014**, *537*, 123–156.

(2) Fang, H. H.; Yang, J.; Feng, J.; Yamao, T.; Hotta, S.; Sun, H. B. Functional organic single crystals for solid-state laser applications. *Laser Photonics Rev.* **2014**, *8*, 687–715.

(3) Aragó, J.; Troisi, A. Dynamics of the Excitonic Coupling in Organic Crystals. *Phys. Rev. Lett.* **2015**, *114*, 1–5.

(4) Gierschner, J.; Varghese, S.; Park, S. Y. Organic Single Crystal Lasers: A Materials View. *Adv. Opt. Mater.* **2016**, *4*, 348–364.

(5) Shi, J.; Aguilar Suarez, L. E.; Yoon, S. J.; Varghese, S.; Serpa, C.; Park, S. Y.; Lüer, L.; Roca-Sanjuán, D.; Milián-Medina, B.; Gierschner, J. Solid State Luminescence Enhancement in π-Conjugated Materials: Unraveling the Mechanism beyond the Framework of AIE/AIEE. *J. Phys. Chem. C* **2017**, *121*, 23166–23183.

(6) Li, Q.; Blancafort, L. A Conical Intersection Model to Explain Aggregation Induced Emission in Diphenyl Dibenzofulvene. *Chem. Commun.* **2013**, *49*, 5966–5968.

(7) Crespo-Otero, R.; Li, Q.; Blancafort, L. Exploring Potential Energy Surfaces for Aggregation-Induced Emission—From Solution to Crystal. *Chem.: Asian J.* **2019**, *14*, 700–714.

(8) Dommett, M.; Rivera, M.; Crespo-Otero, R. How Inter- and Intramolecular Processes Dictate Aggregation-Induced Emission in Crystals Undergoing Excited-State Proton Transfer. *J. Phys. Chem. Lett.* **2017**, *8*, 6148–6153.

(9) Dommett, M.; Rivera, M.; Smith, M. T. H.; Crespo-Otero, R. Molecular and crystalline requirements for solid state fluorescence exploiting excited state intramolecular proton transfer. *J. Mater. Chem. C* **2020**, *8*, 2558–2568.

(10) Peng, Q.; Yi, Y.; Shuai, Z.; Shao, J. Excited state radiationless decay process with Duschinsky rotation effect: Formalism and implementation. *J. Phys. Chem.* **2007**, *126*, 114302.

(11) Gierschner, J.; Lüer, L.; Milián-Medina, B.; Oelkrug, D.; Egelhaaf, H. J. Highly Emissive H-Aggregates or Aggregation-Induced Emission Quenching? The Photophysics of All-Trans Para-Distyrylbenzene. *J. Phys. Chem. Lett.* **2013**, *4*, 2686–2697.

(12) Giannozzi, P. et al. QUANTUM ESPRESSO: a modular and open-source software project for quantum simulations of materials. *Journal of Physics: Condensed Matter* **2009**, *21*, 395502.

(13) Rivera, M.; Dommett, M.; Crespo-Otero, R. ONIOM(QM:QM') Electrostatic Embedding Schemes for Photochemistry in Molecular Crystals. *J. Chem. Theory Comput.* **2019**, *15*, 2504–2516.

(14) Rivera, M.; Dommett, M.; Sidat, A.; Rahim, W.; Crespo-Otero, R. fromage: A library for the study of molecular crystal excited states at the aggregate scale. *J. Comput. Chem.* **2020**, *41*, 1045–1058.

(15) Frisch, M. J. et al. Gaussian 09, Revision D.01. 2009.

(16) Balasubramani, S. G. et al. TURBOMOLE: Modular program suite for *ab initio* quantum-chemical and condensed-matter simulations. *The Journal of Chemical Physics* **2020**, *152*, 184107.

(17) Aradi, B.; Hourahine, B.; Frauenheim, T. DFTB+, a Sparse Matrix-Based Implementation of the DFTB Method. *J. Phys. Chem. B A* **2007**, *111*, 5678–5684.

(18) Levine, B. G.; Coe, J. D.; Martínez, T. J. Optimizing Conical Intersections Without Derivative Coupling Vectors: Application to Multistate Multireference Second-Order Perturbation Theory (MS-CASPT2). *J. Phys. Chem. B* **2008**, *112*, 405–413.

(19) Aquilante, F. et al. Molcas 8: New Capabilities for Multiconfigurational Quantum Chemical Calculations Across the Periodic Table. *J. Comput. Chem.* **2016**, *37*, 506–541.

(20) Crespo-Otero, R.; Barbatti, M. Spectrum simulation and decomposition with nuclear ensemble: Formal derivation and application to benzene, furan and 2-phenylfuran. *Theor. Chem. Acc.* **2012**, *131*, 1–14.

(21) Barbatti, M.; Ruckenbauer, M.; Plasser, F.; Pittner, J.; Granucci, G.; Persico, M.; Lischka, H. Newton-X: A surface-hopping program for nonadiabatic molecular dynamics. *Wiley Interdiscip. Rev. Comput. Mol. Sci.* **2014**, *4*, 26–33.

(22) Reimers, J. R. A practical method for the use of curvilinear coordinates in calculations of normal-mode-projected displacements and duschinsky rotation matrices for large molecules. *J. Chem. Phys.* **2001**, *115*, 9103–9109.

(23) Strickler, S. J.; Berg, R. A. Relationship between Absorption Intensity and Fluorescence Lifetime of Molecules. *J. Chem. Phys.* **1962**, *37*, 814–822.

(24) Stehr, V.; Fink, R. F.; Engels, B.; Pflaum, J.; Deibel, C. Singlet Exciton Diffusion in Organic Crystals Based on Marcus Transfer Rates. *J. Chem. Theory Comput.* **2014**, *10*, 1242–1255.

(25) Kimura, A.; Kakitani, T.; Yamato, T. Theory of Excitation Energy Transfer in the Intermediate Coupling Case. II. Criterion for Intermediate Coupling Excitation Energy Transfer Mechanism and Application to the Photosynthetic Antenna System. *J. Phys. Chem. B* **2000**, *104*, 9276–9287.

(26) Desiraju, G. R.; Gavezzotti, A. Crystal structures of polynuclear aromatic hydrocarbons. Classification, rationalization and prediction from molecular structure. *Acta Crystallogr. B* **1989**, *45*, 473–482.

(27) Campbell, J. E.; Yang, J.; Day, G. M. Predicted Energy–Structure–Function Maps for the Evaluation of Small Molecule Organic Semiconductors. *J. Mater. Chem. C* **2017**, *5*, 7574–7584.

(28) Lee, J.; Kim, C. H.; Joo, T. Active Role of Proton in Excited State Intramolecular Proton Transfer Reaction. *J. Phys. Chem. A* **2013**, *117*, 1400–1405.

(29) Du, M.; Huo, B.; Li, M.; Shen, A.; Bai, X.; Lai, Y.; Liu, J.; Yang, Y. A "Turn-On" fluorescent probe for sensitive and selective detection of fluoride ions based on aggregation-induced emission. *RSC Adv.* **2018**, *8*, 32497–32505.

(30) Pavlopoulos, T. G.; Hammond, P. R. Spectroscopic studies of some laser dyes. *J. Am. Chem. Soc.* **1974**, *96*, 6568–6579.

(31) Katoh, R.; Suzuki, K.; Furube, A.; Kotani, M.; Tokumaru, K. Fluorescence Quantum Yield of Aromatic Hydrocarbon Crystals. *J. Phys. Chem. C* **2009**, *113*, 2961–2965.

(32) Stampfl, J.; Tasch, S.; Leising, G.; Scherf, U. Quantum efficiencies of electroluminescent poly(para-phenylenes). *Synth. Met.* **1995**, *71*, 2125 – 2128.

(33) Kasha, M.; Rawls, H. R.; Ashraf El-Bayoumi, M. The Exciton Model in Molecular Spectroscopy. *Pure Appl. Chem.* **1965**, *11*, 371–392.

(34) Van Hutten, P. F.; Wildeman, J.; Meetsma, A.; Hadziioannou, G. Molecular packing in unsubstituted semiconducting phenylenevinylene oligomer and polymer. *J. Am. Chem. Soc.* **1999**, *121*, 5910–5918.

(35) Fornari, R. P.; Rowe, P.; Padula, D.; Troisi, A. Importance and Nature of Short-Range Excitonic Interactions in Light Harvesting Complexes and Organic Semiconductors. *J. Chem. Theory Comput.* **2017**, *13*, 3754–3763.

(36) Spano, F. C.; Beljonne, D. In *The WSPC Reference on Organic Electronics: Organic Semiconductors*; Bredas, J.-L., Marder, S. R., Eds.; World Scientific: Hackensack, 2016; Chapter 4, pp 93–130.

(37) Chen, Q.; Jia, C.; Zhang, Y.; Du, W.; Wang, Y.; Huang, Y.; Yang, Q.; Zhang, Q. A novel fluorophore based on the coupling of AIE and ESIPT mechanisms and its application in biothiol imaging. *J. Mater. Chem. B* **2017**, *5*, 7736–7742.

(38) Zhang, W.; Sakurai, T.; Aotani, M.; Watanabe, G.; Yoshida, H.; Padalkar, V. S.; Tsutsui, Y.; Sakamaki, D.; Ozaki, M.; Seki, S. Highly Fluorescent Liquid Crystals from Excited-State Intramolecular Proton Transfer Molecules. *Adv. Opt. Mater.* **2019**, *7*, 1801349.

(39) Majumdar, P.; Zhao, J. 2-(2-Hydroxyphenyl)-benzothiazole (HBT)-Rhodamine Dyad: Acid-Switchable Absorption and Fluorescence of Excited-State Intramolecular Proton Transfer (ESIPT). *J. Phys. Chem. B* **2015**, *119*, 2384–2394.

(40) Barbatti, M.; Aquino, A. J. A.; Lischka, H.; Schriever, C.; Lochbrunner, S.; Riedle, E. Ultrafast internal conversion pathway and mechanism in 2-(2'-hydroxyphenyl)benzothiazole: a case study for excited-state intramolecular proton transfer systems. *Phys. Chem. Chem. Phys.* **2009**, *11*, 1406–1415.

(41) Pijeau, S.; Foster, D.; Hohenstein, E. G. Excited-State Dynamics of 2-(2'-Hydroxyphenyl)benzothiazole: Ultrafast Proton Transfer and Internal Conversion. *J. Phys. Chem. A* **2017**, *121*, 4595–4605.

(42) Hu, R.; Li, S.; Zeng, Y.; Chen, J.; Wang, S.; Li, Y.; Yang, G. Understanding the aggregation induced emission enhancement for a compound with excited state intramolecular proton transfer character. *Phys. Chem. Chem. Phys.* **2011**, *13*, 2044–2051.

(43) Brewer, W. E.; Martinez, M. L.; Chou, P. T. Mechanism of the ground-state reverse proton transfer of 2-(2-hydroxyphenyl)benzothiazole. *J. Phys. Chem.* **1990**, *94*, 1915–1918.

(44) Lee, J.; Kim, C. H.; Joo, T. Active Role of Proton in Excited State Intramolecular Proton Transfer Reaction. *J. Phys. Chem. A* **2013**, *117*, 1400–1405.

(45) Zhang, W.; Yan, Y.; Gu, J.; Yao, J.; Zhao, Y. S. Low-Threshold Wavelength-Switchable Organic Nanowire Lasers Based on Excited-State Intramolecular Proton Transfer. *Angew. Chem. Int. Ed.* **2015**, *54*, 7125–7129.

(46) Izquierdo, M. A.; Shi, J.; Oh, S.; Park, S. Y.; Milián-Medina, B.; Gierschner, J.; Roca-Sanjuán, D. Excited-state non-radiative decay in stilbenoid compounds: an ab initio quantum-chemistry study on size and substituent effects. *Phys. Chem. Chem. Phys.* **2019**, *21*, 22429–22439.

(47) Shi, J.; Izquierdo, M. A.; Oh, S.; Park, S. Y.; Milián-Medina, B.; Roca-Sanjuán, D.; Gierschner, J. Inverted energy gap law for the nonradiative decay in fluorescent floppy molecules: larger fluorescence quantum yields for smaller energy gaps. *Org. Chem. Front.* **2019**, *6*, 1948–1954.

(48) Escudero, D. *Photodeactivation Channels of Transition Metal Complexes: A Computational Chemistry Perspective*; Springer International Publishing, 2019; Vol. 29; pp 259–287.

(49) Andreev, A.; Matt, G.; Brabec, C. J.; Sitter, H.; Badt, D.; Seyringer, H.; Sariciftci, N. S. Highly Anisotropically Self-Assembled Structures of para-Sexiphenyl Grown by Hot-Wall Epitaxy. *Adv. Mater.* **2000**, *12*, 629–633.

(50) Duan, Y. et al. Aggregation Induced Enhancement of Linear and Nonlinear Optical Emission from a Hexaphenylene Derivative. *Adv. Funct. Mater.* **2016**, *26*, 8968–8977.

(51) Quochi, F.; Cordella, F.; Mura, A.; Bongiovanni, G.; Balzer, F.; Rubahn, H.-G. Gain amplification and lasing properties of individual organic nanofibers. *Appl. Phys. Lett.* **2006**, *88*, 041106.

(52) Quochi, F.; Andreev, A.; Cordella, F.; Orrú, R.; Mura, A.; Bongiovanni, G.; Hoppe, H.; Sitter, H.; Sariciftci, N. Low-threshold blue lasing in epitaxially grown para-sexiphenyl nanofibers. *J. Lumin.* **2005**, *112*, 321 – 324.

(53) Quochi, F.; Saba, M.; Cordella, F.; Gocalinska, A.; Corpino, R.; Marceddu, M.; Anedda, A.; Andreev, A.; Sitter, H.; Sariciftci, N. S.; Mura, A.; Bongiovanni, G.

Temperature Tuning of Nonlinear Exciton Processes in Self-Assembled Oligophenyl Nanofibers under Laser Action. *Adv. Mater.* **2008**, *20*, 3017–3021.

(54) Mukundam, V.; Dhanunjayarao, K.; Mamidala, R.; Venkatasubbaiah, K. Synthesis, characterization and aggregation induced enhanced emission properties of tetraaryl pyrazole decorated cyclophosphazenes. *J. Mater. Chem. C* **2016**, *4*, 3523–3530.

(55) Tuna, D.; Lefrancois, D.; Wolański, Ł.; Gozem, S.; Schapiro, I.; Andruniów, T.; Dreuw, A.; Olivucci, M. Assessment of Approximate Coupled-Cluster and Algebraic-Diagrammatic-Construction Methods for Ground- and Excited-State Reaction Paths and the Conical-Intersection Seam of a Retinal-Chromophore Model. *J. Chem. Theory Comput.* **2015**, *11*, 5758–5781.

(56) Schapiro, I.; Melaccio, F.; Laricheva, E. N.; Olivucci, M. Using the computer to understand the chemistry of conical intersections. *Photochem. Photobiol. Sci.* **2011**, *10*, 867–886.

Graphical TOC Entry